crystals

MDPI

Article

Synthesis and Thermoelectric Properties of Copper Sulfides via Solution Phase Methods and Spark Plasma Sintering

Yun-Qiao Tang, Zhen-Hua Ge * and Jing Feng

Faculty of Materials Science and Engineering, Kunming University of Science and Technology, Kunming 650093, China; yqt-joe@foxmail.com (Y.-Q.T.); jingfeng@kmust.edu.cn (J.F.)

* Correspondence: zge@kmust.edu.cn

Academic Editor: George S. Nolas

Received: 27 April 2017; Accepted: 13 May 2017; Published: 16 May 2017

Abstract: Large-scale Cu_2S tetradecahedrons microcrystals and sheet-like Cu_2S nanocrystals were synthesized by employing a hydrothermal synthesis (HS) method and wet chemistry method (WCM), respectively. The morphology of α-Cu_2S powders prepared by the HS method is a tetradecahedron with the size of 1–7 μm. The morphology of β-Cu_2S is a hexagonal sheet-like structure with a thickness of 5–20 nm. The results indicate that the morphologies and phase structures of Cu_2S are highly dependent on the reaction temperature and time, even though the precursors are the exact same. The polycrystalline copper sulfides bulk materials were obtained by densifying the as-prepared powders using the spark plasma sintering (SPS) technique. The electrical and thermal transport properties of all bulk samples were measured from 323 K to 773 K. The pure Cu_2S bulk samples sintered by using the powders prepared via HS reached the highest thermoelectric figure of merit (ZT) value of 0.38 at 573 K. The main phase of the bulk sample sintered by using the powder prepared via WCM changed from β-Cu_2S to $Cu_{1.8}S$ after sintering due to the instability of β-Cu_2S during the sintering process. The $Cu_{1.8}S$ bulk sample with a $Cu_{1.96}S$ impurity achieved the highest ZT value of 0.62 at 773 K.

Keywords: Cu_2S; nanocrystal; synthetic methods; morphological control; thermoelectric properties

1. Introduction

Thermoelectric (TE) material is a kind of energy conversion material which takes advantage of solid material internal carriers and phonon interactions to convert thermal and electrical energy directly into each other. The energy crisis and environmental problems have promoted the swift development of TE materials in the past few decades [1–4]. Compared to the mainstream tellurium-based TE materials [5–8], nanostructured metal chalcogenides with low cost, low toxicity, and abundant elements exhibit interesting physical properties [9,10]. Therefore, nanostructured metal chalcogenides TE materials such as Cu-Se [11–13] and Cu-S materials [14–17] have received more attention.

Copper sulfides ($Cu_{2-x}S$ ($0 \leq x \leq 1$)), with different copper stoichiometric ratios, which are a series of compounds ranging from copper-rich Cu_2S to copper deficient CuS, are considered to be superionic conductors [18]. As an important semiconductor, Cu_2S is of high interest due to its unique electronic, thermodynamic, optical, and other physical and chemical properties. It has great potential in a wide range of applications such as thermoelectric materials [19], solar cells [20,21], conductive fibers [22], optical filters [23], and high-capacity cathode materials in lithium secondary batteries [24]. Moreover, Cu_2S nanoparticles with various morphologies have been synthesized by various approaches such as chemical precipitation [25], solventless thermolysis [26], water-oil interface confined method [27], and thermal decomposition [28].

Here, we employed facile solution methods, including hydrothermal synthesis (HS) and wet chemistry method (WCM), to synthesize Cu_2S powders with controllable microstructures under relatively facile conditions. Then, polycrystalline copper sulfides were fabricated by densifying the compound powders using the spark plasma sintering (SPS) technique. The thermoelectric properties of all the bulk samples were measured.

2. Experimental Section

Commercial high-purity powders of CuO (99.9%) and S (99.99%) were used as raw materials. Meanwhile, ethylene diamine (EDA) and hydrazine hydrate ($N_2H_4{\cdot}H_2O$) were used as a chelating agent (EDA) and a reducing agent ($N_2H_4{\cdot}H_2O$), respectively. In a typical wet chemistry method, CuO (10 mmol) and S (20 mmol) were first added to EDA (40 mL) by stirring at room temperature for 10 min. Then, $N_2H_4{\cdot}H_2O$ (35 mL) was dripped slowly into the beaker under further stirring for 12 h at room temperature. The chelating agent EDA reacted with Cu ions to form the complex compounds for avoiding the precipitation of metal Cu. The reducing agent $N_2H_4{\cdot}H_2O$ reduced the Cu^{2+} to Cu^{+} and S to S^{2-}, respectively.

In a typical hydrothermal synthesis [29] method, CuO (10 mmol) and S (20 mmol) were first added to EDA (40 mL), and the mixture was stirred and heated to 373 K for 10 min. After that, $N_2H_4{\cdot}H_2O$ (35 mL) was dripped slowly into the solution under further stirring for 10 min at 373 K. The mixed solution was then transferred into a Teflon-lined stainless steel autoclave (100 mL capacity), which was sealed and maintained at 453 K for 6 h. The final solid products were filtered and washed with DI water and ethanol three times before drying under vacuum at 333 K for 12 h.

The resultant powders were loaded into a graphite die with an inner diameter of 15 mm and then sintered at 773 K for 5 min (heating rate of 100 K/min) under an axial compressive stress of 40 MPa in a vacuum by using a spark plasma sintering (SPS) system (SPS1050; Sumitomo, Tokyo, Japan). The SPS-prepared specimens were disk-shaped with dimensions of Φ15 mm × 4 mm. The phase structure was analyzed by X-ray diffraction with a Cu K_α radiation (λ = 1.5406 Å) filtered through Ni foil (RAD-B system; Rigaku, Tokyo, Japan). The morphologies of the powders and the fracture of the bulk samples were observed by field-emission scanning electron microscopy (FESEM, SUPRA 55, Carl Zeiss, Oberkochen, Germany). The microstructure of the powder was also checked using transmission electron microscopy (TEM, Phililp Tecnai F20, Amsterdam, Dutch). In a typical TEM sample preparation procedure, powders were first added to ethyl alcohol, and stirred for 10 min by ultrasound. Then, the supernatant was dropped on the copper grid.

The electrical transport properties were evaluated along a sample section perpendicular to the SPS pressing direction. The Seebeck coefficient and electrical resistivity were measured from 323 to 773 K in a helium atmosphere using a Seebeck coefficient/electrical resistance measuring system (ZEM-3, Ulvac-Riko, Kanagawa, Japan). The density (d) of the sample was measured by the Archimedes method. In addition, the thermal conductivity of the samples was calculated by the relationship $\kappa = DC_pd$ from the thermal diffusivity D measured by the laser flash method (LFA457; NETZSCH, Selb, Bavaria, Germany).

3. Results and Discussion

3.1. Powder Synthesis and Characterization

3.1.1. XRD Analysis

Figure 1 shows the XRD patterns of Cu_2S powders which prepared by WCM and HS methods. All of the diffraction peaks of the HS sample are well-matched with the standard card of α-Cu_2S (JSPDS no. 83-1462), showing that the pure monoclinic α-Cu_2S powders were obtained by HS methods. All of the diffraction peaks of the WCM sample are well-matched with the standard card β-Cu_2S (JCPDS no. 26-1116), showing that the pure hexagonal β-Cu_2S powders were obtained by WCM.

Actually, the hexagonal β-Cu_2S is high-chalcocite (378–698 K); it would be not stable under thermal shock. The diffraction peaks of powder samples are wider compared to the standard card, indicating the small grain size of the obtained powder. The XRD refinement was performed for the two samples as shown in Figures S1 and S2. The location, proportion and lattice constant of experiment and refinement Cu ions for hexagonal β-Cu_2S powder are shown in Table S1. The proportion of Cu1 changed from 0.75 to 0.4896, indicating that there are more Cu vacancies, smaller lattice parameters, and the possibility of defects in hexagonal Cu_2S.

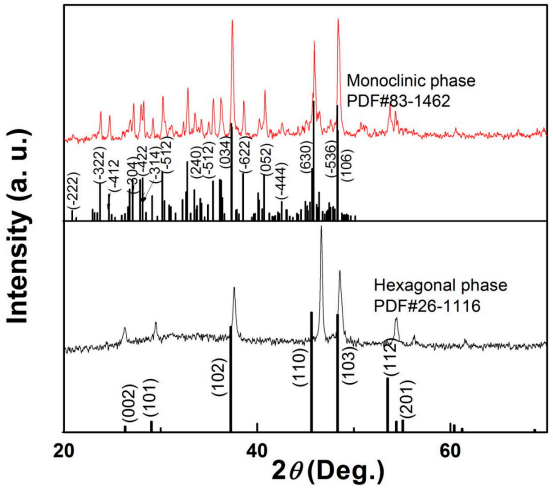

Figure 1. XRD patterns with a selected 2θ range of 20°–70° for Cu_2S powders.

3.1.2. FESEM and TEM Analysis

Figure 2 shows the FESEM images of Cu_2S prepared by different synthesis methods. The pure α-Cu_2S powder which was prepared by the HS method is shown in Figure 2a. The morphology of α-Cu_2S powder prepared by the HS method is a tetradecahedron with the size of 1–7 μm. Figure 2b is a magnified image of a typical single-crystalline α-Cu_2S, shown in Figure 2a. The pure β-Cu_2S powder which was prepared by WCM is shown in Figure 2c. The morphology of hexagonal β-Cu_2S is hexagonal nanosheets. Each nanosheet has an edge length of 10–200 nm and a thickness of 5–20 nm. The morphologies of the powder are highly related to the crystal structure [30]. Similar work reported in the literature for molybdate materials [31] suggests that the synthesis temperature has a strong influence on the morphology of Cu_2S samples. Under the synthesis conditions of high temperature and high pressure, the monoclinic α-Cu_2S showed a tetradecahedron morphology. Also, under relatively mild synthesis conditions (WCM), the hexagonal β-Cu_2S nanosheets were synthesized at room temperature.

The high magnification FEM image of β-Cu_2S is shown in Figure 2d. The β-Cu_2S has a hexagonal sheet-like structure with a thickness of 20 nm. The TEM image (Figure 3a) and selected area of electron diffraction (SAED) patterns (Figure 3b) of a single crystal α-Cu_2S revealed a tetradecahedron Cu_2S of 1 μm in width. The SAED pattern for the tetradecahedron particles (Figure 2b) indicated a highly crystallized monoclinic structure of the α-Cu_2S. Additionally, the TEM image (Figure 3c) and SAED patterns (Figure 3d) of a single-crystalline β-Cu_2S revealed a sheet-like Cu_2S of 10–200 nm in width and of 5–20 nm in thickness. The results are in agreement with SEM observations.

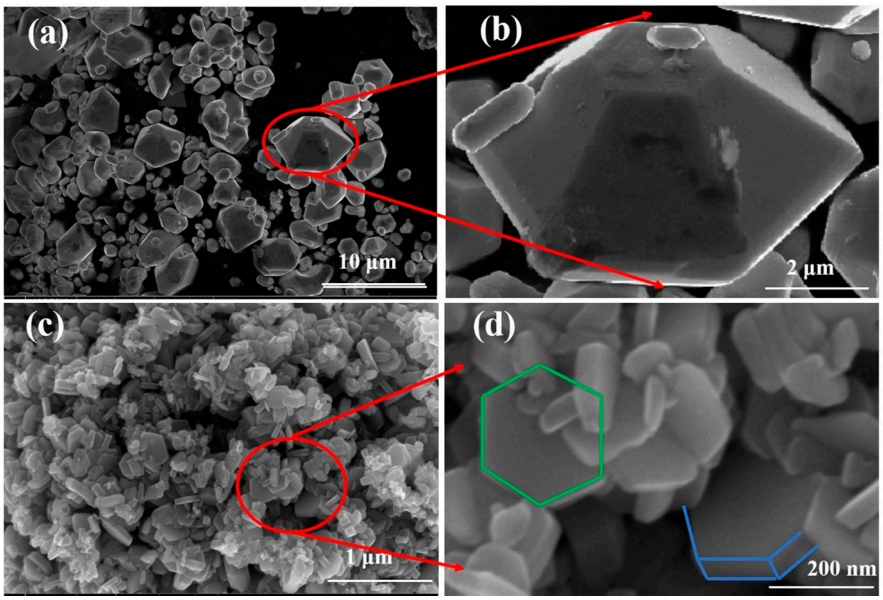

Figure 2. Field emission scanning electron microscopy patterns of the powders under different magnifications. (**a**,**b**) Cu_2S powders prepared by HS; (**c**,**d**) Cu_2S powders prepared by WCM.

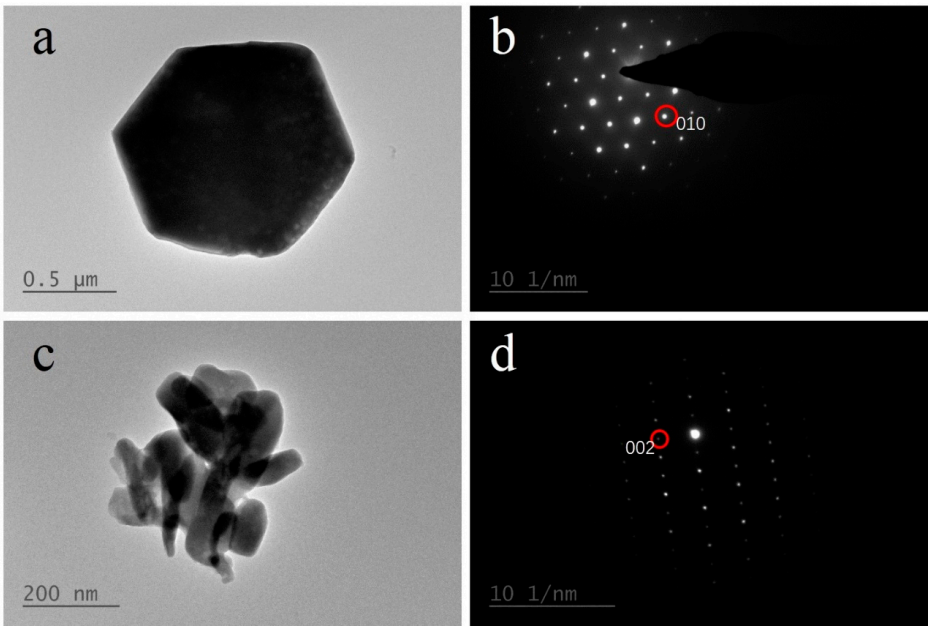

Figure 3. TEM image and SAED patterns for HS-Cu_2S powder (**a**,**c**) and WCM-Cu_2S powder (**b**,**d**).

3.1.3. Synthesis Mechanism

The synthesis process and mechanism of Cu_2S, similar to the flower-like α-Fe_2O_3 reported by Penki et al. [32], were investigated in detail, as shown in Figure 4. The raw CuO (black) and S (yellow) were mixed in a $N_2H_4 \cdot H_2O$ and EDA solution to initially produce the precursor Cu_2O and S^{2-}, and then further react to become the product Cu_2S under the different reaction conditions. When the HS method was employed, the reaction temperature was 453 K and the product was monoclinic α-Cu_2S, as indicated in XRD shown in Figure 1. After 6 h of hydrothermal reaction, the single crystal monoclinic α-Cu_2S formed a tetradecahedron with a dimension of several micrometers as shown in Figure 2a. But when WCM was employed with a reaction temperature of room temperature, the product was hexagonal β-Cu_2S, as indicated in XRD shown in Figure 1. After a 12-h reaction,

the single crystal hexagonal β-Cu_2S grew to form nanosheets with an edge length of 10–200 nm and thickness of 5–20 nm as shown in Figure 2c. The reaction process can be described by Equations (1)–(3).

$$2CuO + 2N_2H_4 \cdot H_2O \rightarrow Cu_2O + 2NH_4^+ + H_2O + 2OH^- + N_2\uparrow \quad (1)$$

$$S + 2N_2H_4 \cdot H_2O \rightarrow S^{2-} + 2NH_4^+ + 2H_2O + N_2\uparrow \quad (2)$$

$$2Cu_2O + 2S^{2-} + 2H_2O \rightarrow 2Cu_2S + 4OH^- \quad (3)$$

Finally, it is suggested that the morphologies and phase structures of Cu_2S are highly dependent on the reaction temperature and time, even if precursors are exactly the same.

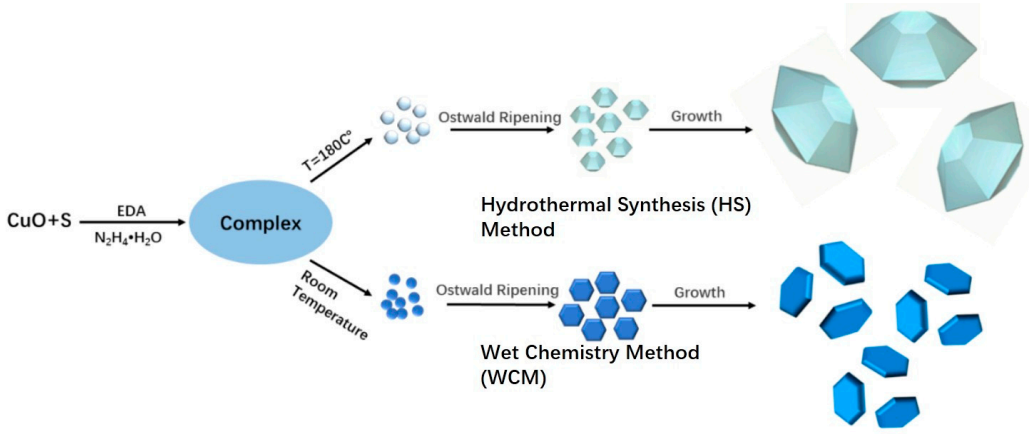

Figure 4. Schematic illustration of the growth mechanism of the Cu_2S powders synthesized by the WCM and HS methods.

3.2. Bulk Characterization

3.2.1. XRD and FESEM Analysis

The bulk sample abbreviated as HS-bulk was prepared by applying SPS at 773 K for 5 min using monoclinic α-Cu_2S powders. The bulk sample abbreviated as WCM-bulk was prepared by applying SPS at 773 K for 5 min using hexagonal β-Cu_2S powders. The XRD patterns of those bulk samples are shown in Figure 5a. The green arrows index the impurity peaks of $Cu_{1.96}S$. The HS-bulk is still in the α-Cu_2S phase. The SEM image of HS-bulk shown in Figure 5b shows a high relative density of 96% and an average grain size of 5 μm, which is very similar to the powders formed by the rapid sintering process. SPS is a rapid sintering technology, after which the nanoscale particles can be maintained in bulk [14]. As shown in the XRD pattern (Figure 5a), the WCM-bulk exhibits a main phase of $Cu_{1.8}S$ with an impurity of $Cu_{1.96}S$. The hexagonal β-Cu_2S is in the high-chalcocite phase, which is instable during the sintering process. Because of thermal shock in the SPS process, the phase transition occurred from β-Cu_2S to $Cu_{1.8}S$, which is the most stable phase in the Cu-S system. Cu_2S is a superionic conductor, and the superionic phase transition temperature is over 689 K [33]. In the SPS sintering program, the sintering temperature is 773 K, and the Cu ions show liquid behavior under this temperature. The extra Cu may precipitate on the anode and be removed during the polishing and cutting process. As shown in Figure 5c, the WCM-bulk sample with a relative density of 90.2% has an average size of 200 nm.

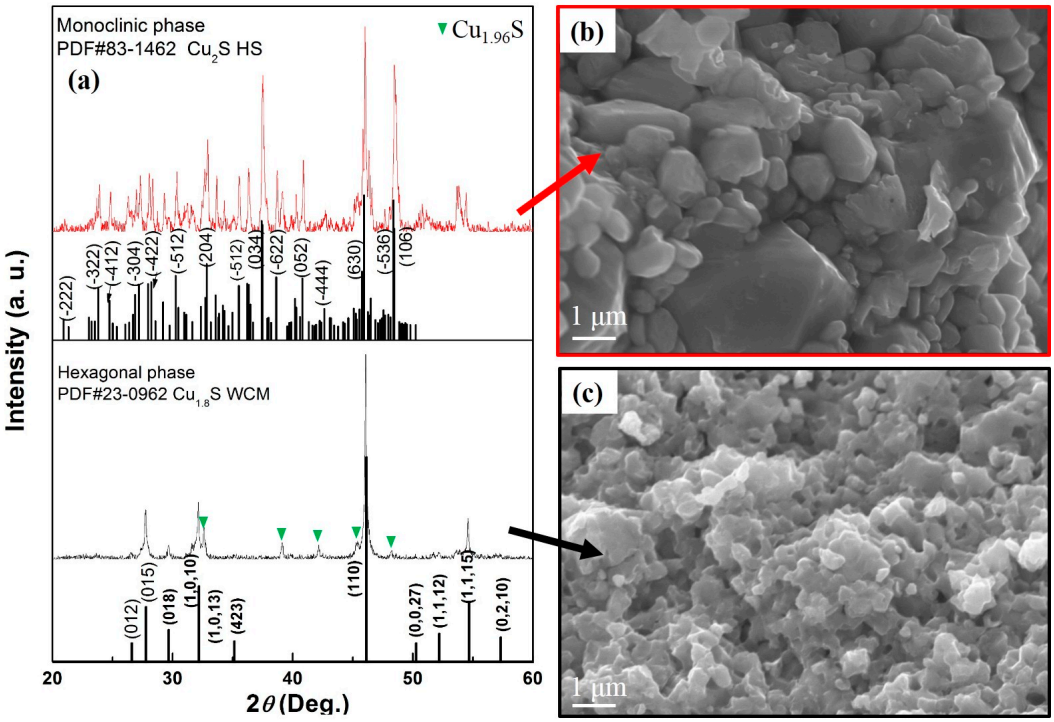

Figure 5. XRD patterns with a selected 2θ range of 20°–70° for bulk samples prepared by SPS at 773 K for 5 min, and field emission scanning electron microscopy of the fractured surfaces for the bulk samples. (**a**) XRD patterns of the two bulk samples; (**b**) FESEM image of HS-bulk; (**c**) FESEM image of WCM-bulk.

3.2.2. Thermoelectric Transport Properties

The TE properties of the two bulk samples were measured. The TE properties of $Cu_{1.8}S$ bulk sample in the literature [34], which were prepared by the same SPS process but using the mechanical alloying (MA) treated powders, are shown for comparison. Figure 6a illustrates the temperature dependence of electrical conductivity (σ) for the bulk samples. As shown in Figure 6a, the HS-bulk has the highest σ value up to 218 Scm^{-1} at 373 K, and WCM-bulk has the highest σ value up to 2490 Scm^{-1} at 373 K. Both the HS-bulk and the WCM-bulk have lower σ than the MA-bulk. The WCM-bulk has a similar main phase to the MA-bulk but a low relative density and impurity of $Cu_{1.96}S$, which decrease the σ value. The HS-bulk sample has the main phase of Cu_2S, while the electrical conductivity of $Cu_{2-x}S$ depends on the Cu content due to its superionic behavior. Therefore, the HS-bulk sample has the lowest electrical conductivity. The WCM-bulk sample has one turning point in the σ curve due to the one phase transition of $Cu_{1.8}S$ during the measured temperature range of 323 K to 773 K [34]. Two turning points in the σ curve were observed for the HS-bulk sample due to the two phase transitions of Cu_2S during the measured temperature range. As reported by Li et al., bulk Cu_2S exhibits three phases (α-phase, β-phase, γ-phase) in the temperature ranges of >698, 378–698, and <378 K [35,36], respectively. The high temperature region to the right of the blue dashed line in Figures 6 and 7 is the γ-phase.

The positive Seebeck coefficient (α) in Figure 6b indicates all bulks are *p*-type semiconductors. According to the equations $\sigma = e\mu n$, and $\alpha \approx \gamma - \ln n$, [37] where σ, μ, n, α and γ are electrical conductivity, carrier mobility, carrier concentration, Seebeck coefficient and scattering factor, respectively, α is usually inversely proportional to σ. The HS-bulk achieved the largest α value of 532 μVK^{-1} at 673 K. The WCM-bulk achieved the largest α value of 101 μVK^{-1} at 773 K. The *PF* was calculated by $PF = \alpha^2\sigma$ and is shown in Figure 6c. The *PF* of the HS-bulk reaches 196 $\mu Wm^{-1}K^{-2}$ at 573 K, and that of the WCM-bulk achieved 985 $\mu Wm^{-1}K^{-2}$ at 773 K.

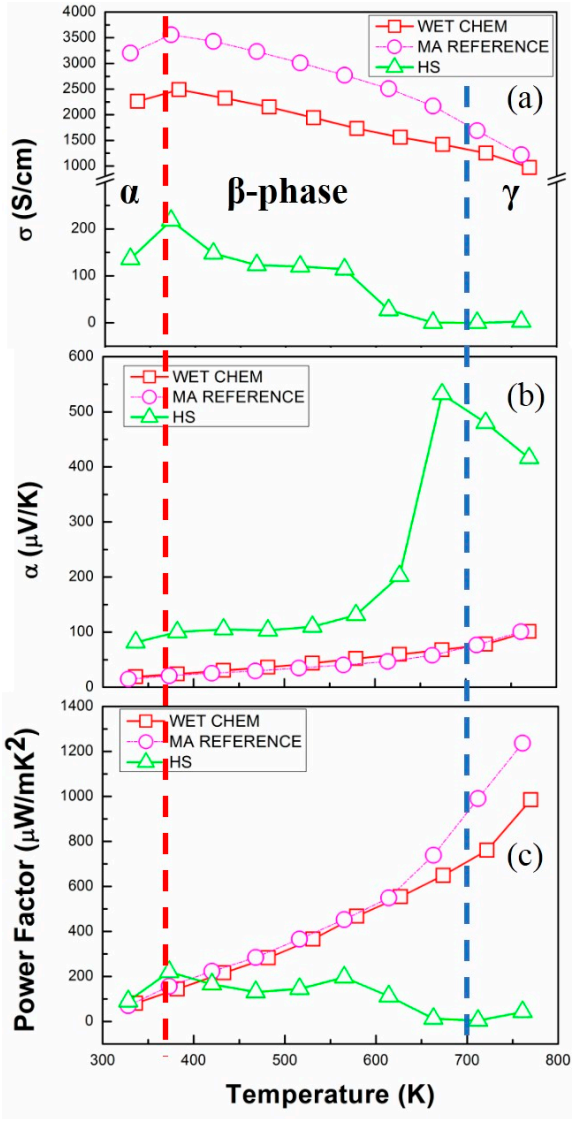

Figure 6. Temperature dependence of electrical conductivity (**a**); Seebeck coefficient (**b**); and power factor (**c**) for the two bulk samples and the reference [34].

Figure 7 shows the temperature dependence of thermal conductivity (κ) (a) and the thermoelectric figure of merit, ZT (b). The κ value of the HS-bulk and the WCM-bulk are lower than that of the MA-bulk [34], due to the fine grain size and the lower relative density. The HS-bulk sample obtained the lowest κ value of 0.20 WmK^{-1} at 673 K. The WCM-bulk sample obtained the lowest κ value of 1.23 WmK^{-1} at 773 K. The κ curve of the HS sample also has two turning points according to the two phases transitions of Cu_2S, which are also similar to the previous report by He et al. [33]. Based on the above measurement results, the ZT was calculated by $ZT = \sigma\alpha^2 T/\kappa$ as shown in Figure 7b. The highest ZT value of 0.38 was obtained at 573 K for the HS-bulk sample, and the WCM-bulk sample obtained the highest ZT value of 0.62 at 773 K. This shows that Cu_2S is a promising thermoelectric material, and the method combining the solution phase method and SPS may be an efficient route for synthesizing high performance bulk TE materials [37].

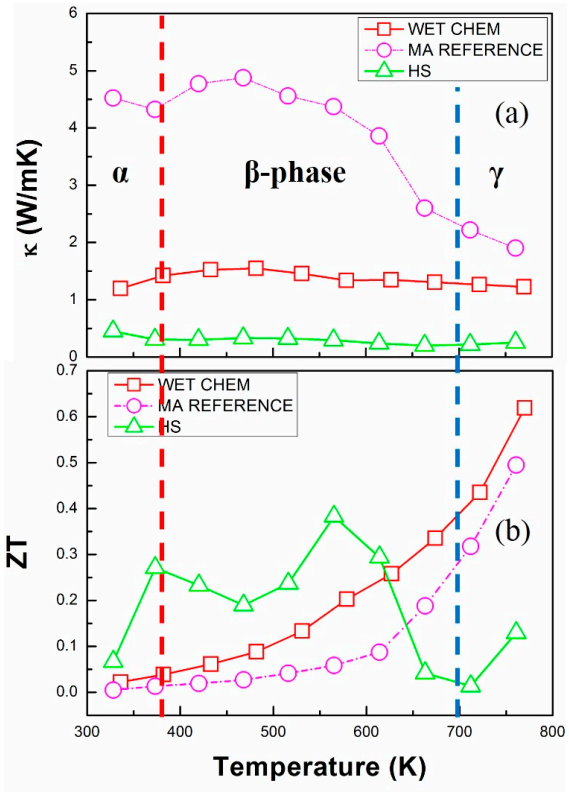

Figure 7. Temperature dependence of thermal conductivity (**a**) for the two bulk samples and *ZT* value and (**b**) for the two bulk samples and the reference [34].

4. Conclusions

The stable solution phase processes for preparing the single phase Cu_2S powders were obtained. Large-scale Cu_2S tetradecahedron microcrystals with monoclinic symmetry and sheet-like Cu_2S nanocrystals with hexagonal β-Cu_2S symmetry were synthesized by employing the hydrothermal synthesis (HS) method and the wet chemistry method (WCM), respectively. The Cu_2S nanopowders were densified to bulk by SPS. Due to the fine grains, low thermal conductivity was achieved, resulting in enhanced TE properties. The highest ZT value of 0.38 was obtained at 573 K for the HS-bulk sample, which is better than the values achieved by the other two samples in this temperature. The WCM-bulk sample obtained the highest ZT value of 0.62 at 773 K. Compared with the MA-bulk [34], the WCM-bulk has a 26.53% increase of ZT value at 773 K. Our work indicated that the morphologies and phase structures of Cu_2S are highly dependent on the reaction temperature and time even when the raw materials were exactly the same.

Supplementary Materials: The following are available online at http://www.mdpi.com/2073-4352/7/5/141/s1, Figure S1: XRD refinement patterns of the hexagonal Cu2S powder sample, Figure S2: XRD refinement patterns of the monoclinic Cu2S powder sample, Table S1: The location, proportion and lattice constant of Cu ions, Table S2: The lattice constant of monoclinic Cu2S powder sample.

Acknowledgments: This work was supported by the National Natural Science Foundation of China (Grant No. 51501086).

Author Contributions: All authors participated in the research, analysis and writing of the manuscript. Zhen-Hua Ge designed the experiments and Yun-Qiao Tang fabricated the samples, preformed the thermoelectric properties characterization and wrote the paper.

Conflicts of Interest: The authors declare no conflicts of interest.

References

1. Sales, B.C. Smaller is cooler. *Science* **2001**, *295*, 1248–1249. [CrossRef] [PubMed]
2. Sootsman, J.R.; Chung, D.Y.; Kanatzidis, M.G. New and old concepts in thermoelectric materials. *Angew. Chem. Int. Ed.* **2009**, *48*, 8616–8639. [CrossRef] [PubMed]
3. Snyder, G.J.; Eric, S.T. Complex thermoelectric materials. *Nat. Mater.* **2008**, *7*, 105–114. [CrossRef] [PubMed]
4. Di Salvo, F.J. Thermoelectric Cooling and Power Generation. *Science* **1999**, *285*, 703–706. [CrossRef]
5. Zhao, X.B.; Ji, X.H.; Zhang, Y.H.; Zhu, T.J.; Tu, J.P.; Zhang, X.B. Bismuth telluride nanotubes and the effects on the thermoelectric properties of nanotube-containing nanocomposites. *Appl. Phys. Lett.* **2005**, *86*, 062111. [CrossRef]
6. Zhang, Y.C.; Wang, H.; Kraemer, S.; Shi, Y.F.; Zhang, F.; Snedaker, M.; Ding, K.; Moskovits, M.; Snyder, G.J.; Stucky, G.D. Surfactant-Free Synthesis of Bi_2Te_3-Te Micro-Nano Heterostructure with Enhanced Thermoelectric Figure of Merit. *ACS Nano* **2011**, *5*, 3158–3165. [CrossRef] [PubMed]
7. Heremans, J.P.; Jovovic, V.; Toberer, E.S.; Saramat, A.; Kurosaki, K.; Charoenphakdee, A.; Yamanaka, S.; Snyder, G.J. Enhancement of thermoelectric efficiency in PbTe by distortion of the electronic density of states. *Science* **2008**, *321*, 554–557. [CrossRef] [PubMed]
8. Li, Z.Y.; Li, J.F.; Zhao, W.Y.; Tan, Q.; Wei, T.R.; Wu, C.F.; Xing, Z.B. PbTe-based thermoelectric nanocomposites with reduced thermal conductivity by SiC nanodispersion. *Appl. Phys. Lett.* **2014**, *104*, 113905. [CrossRef]
9. Gao, M.R.; Xu, Y.F.; Jiang, J.; Yu, S.H. Nanostructured metal chalcogenides: Synthesis, modification, and applications in energy conversion and storage devices. *Chem. Soc. Rev.* **2013**, *42*, 2986–3017. [CrossRef] [PubMed]
10. Ge, Z.H.; Nolas, G.S. Controllable Synthesis of Bismuth Chalcogenide Core–shell Nanorods. *Cryst. Growth Des.* **2014**, *14*, 533–536. [CrossRef]
11. Liu, H.L.; Shi, X.; Xu, F.F.; Zhang, L.L.; Zhang, W.Q.; Chen, L.D.; Uher, C.; Day, T.; Snyder, G.J. Copper ion liquid-like thermoelectrics. *Nat. Mater.* **2012**, *11*, 422–425. [CrossRef] [PubMed]
12. Li, D.; Qin, X.Y.; Liu, Y.F.; Song, C.J.; Wang, L.; Zhang, J.; Xin, H.X.; Guo, G.L.; Zou, T.H.; Sun, G.L.; et al. Chemical synthesis of nanostructured Cu_2Se with high thermoelectric performance. *RSC Adv.* **2014**, *4*, 8638–8644. [CrossRef]
13. Shi, X.; Xi, L.; Fan, J.; Zhang, W.; Chen, L. Cu-Se bond network and thermoelectric compounds with complex diamondlike structure. *Chem. Mater.* **2010**, *22*, 6029–6031. [CrossRef]
14. Ge, Z.H.; Zhang, B.P.; Chen, Y.X.; Yu, Z.X.; Liu, Y.; Li, J.F. Synthesis and transport property of $Cu_{1.8}S$ as a promising thermoelectric compound. *Chem. Commun.* **2011**, *47*, 12697–12699. [CrossRef] [PubMed]
15. Dennler, G.; Chmielowski, R.; Jacob, S.; Capet, F.; Roussel, P.; Zastrow, S.; Nielsch, K.; Opahle, I.; Madsen, G.K.H. Are binary copper sulfides/selenides really new and promising thermoelectric materials? *Adv. Energy Mater.* **2014**, *4*, 1301581. [CrossRef]
16. Abdullaev, G.B.; Aliyarova, Z.A.; Zamanova, E.H.; Asadov, G.A. Investigation of the electric properties of Cu2S single crystals. *Phys. Status Solidi* **1968**, *26*, 65–68. [CrossRef]
17. Lu, X.; Morelli, D.T.; Xia, Y.; Zhou, F.; Ozolins, V.; Chi, H.; Zhou, X.Y.; Uher, C. High Performance Thermoelectricity in Earth-Abundant Compounds Based on Natural Mineral Tetrahedrites. *Adv. Energy Mater.* **2013**, *3*, 342–348. [CrossRef]
18. Miller, T.A.; Wittenberg, J.S.; Wen, H.; Connor, S.; Cui, Y.; Lindenberg, A.M. The mechanism of ultrafast structural switching in superionic copper (I) sulphide nanocrystals. *Nat. Commun.* **2013**, *4*, 1369. [CrossRef] [PubMed]
19. El Akkad, F.; Mansour, B.; Hendeya, T. Electrical and thermoelectric properties of Cu_2Se and Cu_2S. *Mater. Res. Bull.* **1981**, *16*, 535–539. [CrossRef]
20. Rothwarf, A. The CdS/Cu_2S solar cell: Basic operation and anomalous effects. *Sol. Cells* **1980**, *2*, 115–140. [CrossRef]
21. Hall, R.B.; Meakin, J.D. The design and fabrication of high efficiency thin film CdS/Cu2S solar cells. *Thin Solid Films* **1979**, *63*, 203–211. [CrossRef]
22. Kim, S.; Kim, S.; Kim, Y.H.; Ku, B.C.; Jeong, Y. Enhancement of electrical conductivity of carbon nanotube fibers by copper sulfide plating. *Fibers Polym.* **2015**, *16*, 769–773. [CrossRef]
23. Fernandez, A.M.; Nair, M.T.S.; Nair, P.K. Chemically deposited ZnS-NiS-CuS optical filters with wide range solar control characteristics. *Mater. Manuf. Process* **1993**, *8*, 535–548. [CrossRef]

24. Lai, C.H.; Huang, K.W.; Cheng, J.H.; Lee, C.Y.; Hwang, B.J.; Chen, L.J. Direct growth of high-rate capability and high capacity copper sulfide nanowire array cathodes for lithium-ion batteries. *J. Mater. Chem.* **2010**, *20*, 6638–6645. [CrossRef]
25. Wu, S.X.; Jiang, J.; Liang, Y.G.; Yang, P.; Niu, Y.; Chen, Y.D.; Xia, J.F.; Wang, C. Chemical Precipitation Synthesis and Thermoelectric Properties of Copper Sulfide. *J. Electron. Mater.* **2017**, *46*, 2432–2437. [CrossRef]
26. Sigman, M.B.; Ghezelbash, A.; Hanrath, T.; Saunders, A.E.; Lee, F.; Korgel, B.A. Solventless synthesis of monodisperse Cu2S nanorods, nanodisks, and nanoplatelets. *J. Am. Chem. Soc.* **2003**, *125*, 16050–16057. [CrossRef] [PubMed]
27. Zhuang, Z.B.; Peng, Q.; Zhang, B.; Li, Y.D. Controllable synthesis of Cu2S nanocrystals and their assembly into a superlattice. *J. Am. Chem. Soc.* **2008**, *130*, 10482–10483. [CrossRef] [PubMed]
28. Liu, Z.P.; Xu, D.; Liang, J.B.; Shen, J.M.; Zhang, S.Y.; Qian, Y.T. Growth of Cu2S ultrathin nanowires in a binary surfactant solvent. *J. Phys. Chem.* **2005**, *109*, 10699–10704. [CrossRef] [PubMed]
29. Yin, C.Y.; Minakshi, M.; Ralph, D.E.; Jiang, Z.T.; Xie, Z.H.; Guo, H. Hydrothermal synthesis of cubic α-fe$_2$O$_3$, microparticles using glycine: Surface characterization, reaction mechanism and electrochemical activity. *J. Alloys Compd.* **2011**, *509*, 9821–9825. [CrossRef]
30. Zhang, Y.Q.; Zhang, B.P.; Ge, Z.H.; Zhu, L.F.; Li, Y. Preparation by solvothermal synthesis, growth mechanism, and photocatalytic performance of CuS nanopowders. *Eur. J. Inorg. Chem.* **2014**, *2014*, 2368–2375. [CrossRef]
31. Barmi, M.J.; Minakshi, M. Tuning the redox properties of the nanostructured $CoMoO_4$ electrode: Effects of surfactant content and synthesis temperature. *ChemPlusChem* **2016**, *81*, 964–977. [CrossRef]
32. Penki, T.R.; Shivakumara, S.; Minakshi, M.; Munichandraiah, N. Porous Flower-like α-Fe_2O_3 Nanostructure: A High Performance Anode Material for Lithium-ion Batteries. *Electrochim. Acta* **2015**, *167*, 330–339. [CrossRef]
33. He, Y.; Day, T.; Zhang, T.S.; Liu, H.L.; Shi, X.; Chen, L.D.; Snyder, G.J. High Thermoelectric Performance in Non-Toxic Earth-Abundant Copper Sulfide. *Adv. Mater.* **2014**, *26*, 3974–3978. [CrossRef] [PubMed]
34. Ge, Z.H.; Liu, X.Y.; Feng, D.; Lin, J.Y.; He, J.Q. High-Performance Thermoelectricity in Nanostructured Earth-Abundant Copper Sulfides Bulk Materials. *Adv. Energy Mater.* **2016**, *6*, 1600607. [CrossRef]
35. Li, B.; Huang, L.; Zhao, G.Y.; Wei, Z.M.; Dong, H.L.; Hu, W.P.; Wang, L.W.; Li, J.B. Large-Size 2D β-Cu_2S Nanosheets with Giant Phase Transition Temperature Lowering (120 K) Synthesized by a Novel Method of Super-Cooling Chemical-Vapor-Deposition. *Adv. Mater.* **2016**, *28*, 8271–8276. [CrossRef] [PubMed]
36. Okamoto, K.; Kawai, S. Electrical conduction and phase transition of copper sulfides. *Jpn. J. Appl. Phys.* **1973**, *12*, 1130. [CrossRef]
37. Ge, Z.H.; Zhao, L.D.; Wu, D.; Zhang, B.P.; Li, J.F.; He, J.Q. Low cost, abundant binary sulfides as promising thermoelectric. *Mater. Today* **2016**, *19*, 227–239. [CrossRef]